

## SIMULATION OF THE CROSSHOLE METHOD IN ISOTROPIC AND ANISOTROPIC MEDIA

SEONG-MIN KIM<sup>1\*†</sup>, SHU-TAO LIAO<sup>2‡</sup>, AND JOSE M. ROESSET<sup>3§</sup>

<sup>1</sup> *Department of Civil Engineering, The University of Texas at Austin, Austin, TX 78712, U.S.A.*

<sup>2</sup> *Department of Civil Engineering, Chung-Hua University, Hsin-Chu 30067, Taiwan*

<sup>3</sup> *Department of Civil Engineering, The University of Texas at Austin, Austin, TX 78712, U.S.A.*

### SUMMARY

The crosshole seismic method was simulated using a finite element model with a diagonal mass matrix and a direct integration of the equations of motion in the time domain. The results were compared to those of a more efficient but also more restricted formulation using discrete Green's functions. The effects of the type of excitation, the shape of the applied pulse and the position of the receiver with respect to the source on the shape of the recorded motions were investigated for isotropic and cross anisotropic soil deposits. The computed times of arrival of the different waves were compared to those predicted using curved ray path theory to assess the accuracy of this much simpler procedure as a means to interpret the experimental data and determine the soil properties. Copyright © 1999 John Wiley & Sons, Ltd.

KEY WORDS: cross anisotropy; crosshole method; finite element; Green's function; ray path

### INTRODUCTION

The crosshole method is a commonly used procedure to determine the material properties of soil deposits *in situ* and their variation with depth.<sup>1</sup> In this method a source is placed at various elevations down a borehole and the motions are recorded at one or two parallel boreholes. The receivers are normally placed at the same depth as the source but they can also be placed at other elevations when performing tomography. From the records obtained the velocities of propagation of the different types of waves are generally obtained assuming simple ray path theory, and often straight ray paths.

The crosshole seismic method was simulated numerically in this study using a finite model of the soil. The convergence of the solution as a function of the mesh size was investigated and the results were compared to those of a more efficient but also more restricted solution in the frequency domain using the discrete Green's functions proposed Kauser.<sup>2</sup> The shapes of the motions recorded at various depths as functions of the type of excitation and the shape of the pulse were studied next to identify the times of arrival of SH, SV and P waves as appropriate. The times of arrival of the waves were also obtained using a curved ray path model and the results

\* Correspondence to: Seong-Min Kim, Research Associate, Center for Transportation Research, The University of Texas at Austin, 3208 Red River, Suite 200, Austin, TX 78705, USA

† Research Associate

‡ Associate Professor

§ Joe J. King Chair in Engineering

were compared with those obtained with the finite element model. The effect of soil cross anisotropy when the material properties are the same in the two horizontal directions but different in the vertical direction was finally investigated. The main objective of the work was to assess the possibility of backcalculating material constants from crosshole tests illustrating some of the difficulties involved in identifying the times of arrival of the different waves.

### FINITE ELEMENT FORMULATION

The soil surrounding the source borehole was modelled using four noded, linear isoparametric, axisymmetric finite elements in cylindrical coordinates with a Fourier expansion in the circumferential direction. Three types of excitations were considered as shown in Figure 1. PT, VS and RE forces were represented by a pure torsional force, a vertical shear force uniformly distributed over a ring and a uniformly distributed radial expansion or contraction, respectively. For all 3 cases it is only necessary to consider the  $n = 0$  (axisymmetric) term of the Fourier expansion. It should be noted that because the simulation used axisymmetric finite elements, the receiver borehole could not be modelled and the interaction of the waves with the receiver borehole was ignored.

For the pure torsion (PT excitation) the radial and vertical displacements are zero and only the strains  $\gamma_{r\theta}$  and  $\gamma_{rz}$  need to be considered with the tangential displacement  $v$  and loads  $P_\theta$ . For the vertical shear forces (VS excitation) or the radial pressure (RE excitation) the tangential displacement would be 0 as well as the two shear strains  $\gamma_{r\theta}$  and  $\gamma_{rz}$ . The radial displacement  $u$ , the vertical  $w$  and the strains  $\varepsilon_r$ ,  $\varepsilon_\theta$ ,  $\varepsilon_z$ ,  $\gamma_{rz}$  and forces  $P_r$  and  $P_z$  are independent of the azimuthal angle  $\theta$ .

The constitutive law for a cross anisotropic material, assuming the  $r\theta$  (horizontal) plane to be the isotropic plane, is defined by

$$\sigma = \mathbf{D}\varepsilon, \text{ or } \begin{pmatrix} \sigma_r \\ \sigma_\theta \\ \sigma_z \\ \tau_{r\theta} \\ \tau_{\theta z} \\ \tau_{zr} \end{pmatrix} = \begin{bmatrix} M_H & C_{12} & C_{13} & 0 & 0 & 0 \\ C_{12} & M_H & C_{13} & 0 & 0 & 0 \\ C_{13} & C_{13} & M_V & 0 & 0 & 0 \\ 0 & 0 & 0 & G_{HH} & 0 & 0 \\ 0 & 0 & 0 & 0 & G_{VH} & 0 \\ 0 & 0 & 0 & 0 & 0 & G_{VH} \end{bmatrix} \begin{pmatrix} \varepsilon_r \\ \varepsilon_\theta \\ \varepsilon_z \\ \gamma_{r\theta} \\ \gamma_{\theta z} \\ \gamma_{zr} \end{pmatrix} \quad (1)$$

where,  $\mathbf{D}$  is the material property matrix,  $M_H$  and  $M_V$  are the constrained moduli in the isotropic and anisotropic planes,  $G_{HH}$  and  $G_{VH}$  are the shear moduli in the isotropic and anisotropic planes and  $C_{12}$  is equal to  $M_H - 2G_{HH}$ . The fifth elastic constant  $C_{13}$  is defined in this study for cross anisotropic problems as<sup>3</sup>

$$C_{13} = \alpha \left( \frac{M_H + M_V}{2} - 2G_{HH} \right) \text{ with } \alpha = \frac{1}{2} \quad (2)$$

For isotropic media with  $M_H = M_V = M$  and  $G_{HH} = G_{VH} = G$ , or  $\alpha$  would have a value of 1 and  $C_{13}$  would be equal to the Lamé constant  $\lambda$  ( $M = \lambda + 2G$ ).

After forming the consistent mass matrix of each element it was diagonalized using the criterion proposed by Hinton *et al.*<sup>4</sup> If  $M_{ij}$  is the  $i$ th row and  $j$ th column entry, the diagonal terms of the

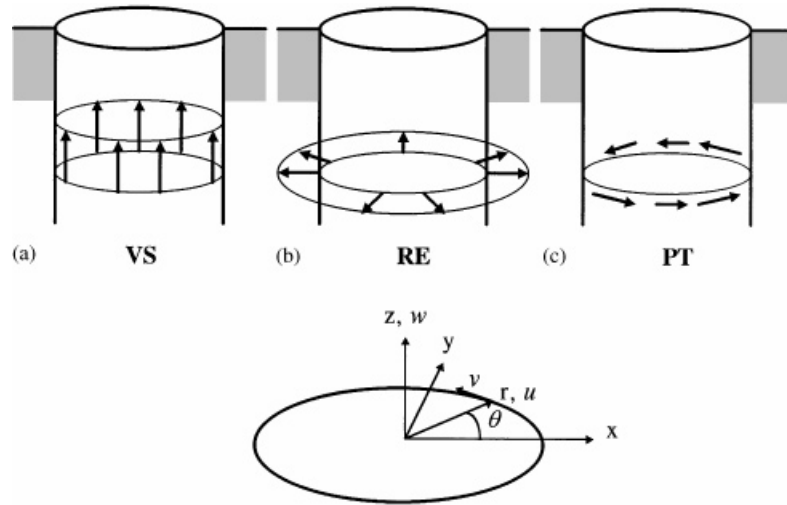


Figure 1. Types of excitations: (a) vertical shear force (VS); (b) radial expansion (RE); (c) pure torsional force (PT)

new mass matrix are

$$M_{ii}^* = \frac{M_{ii}}{\sum_{i=1}^n M_{ii}} \left( \sum_{i=1}^n \sum_{j=1}^n M_{ij} \right) \quad (3)$$

where  $n$  is the total number of degrees of freedom in an element.

The central difference method was used for the dynamic analysis. The equilibrium equations for linear dynamic responses of finite element systems can be expressed by

$$\mathbf{M}\ddot{\mathbf{U}}_t + \mathbf{C}\dot{\mathbf{U}}_t + \mathbf{K}\mathbf{U}_t = \mathbf{P}_t \quad (4)$$

where  $\mathbf{U}_t$ ,  $\dot{\mathbf{U}}_t$ ,  $\ddot{\mathbf{U}}_t$  and  $\mathbf{P}_t$  are the displacement, velocity, acceleration, and external load vectors of the finite element assemblage at time  $t$ .  $\mathbf{M}$ ,  $\mathbf{C}$ , and  $\mathbf{K}$  are the mass, damping, and stiffness matrices. If  $\Delta t$  is the time step,  $\mathbf{U}_{t+1} = \mathbf{U}(t + \Delta t)$ , and  $\mathbf{U}_{t-1} = \mathbf{U}(t - \Delta t)$ , the velocity and acceleration can be estimated by

$$\ddot{\mathbf{U}}_t = \frac{1}{2\Delta t}(\mathbf{U}_{t+1} - \mathbf{U}_{t-1}), \quad \text{and} \quad \dot{\mathbf{U}}_t = \frac{1}{\Delta t^2}(\mathbf{U}_{t+1} - 2\mathbf{U}_t + \mathbf{U}_{t-1}) \quad (5)$$

Substituting (5) into (4) yields

$$\mathbf{U}_{t+1} = \mathbf{H}_{-1}(\mathbf{P}_t - \mathbf{K}\mathbf{U}_t) + \frac{2}{\Delta t^2}\mathbf{H}^{-1}\mathbf{M}\mathbf{U}_t + \mathbf{H}^{-1}\left(\frac{1}{2\Delta t}\mathbf{C} - \frac{1}{\Delta t^2}\mathbf{M}\right)\mathbf{U}_{t-1} \quad (6)$$

where

$$\mathbf{H} = \frac{1}{\Delta t^2}\mathbf{M} + \frac{1}{2\Delta t}\mathbf{C} \quad (7)$$

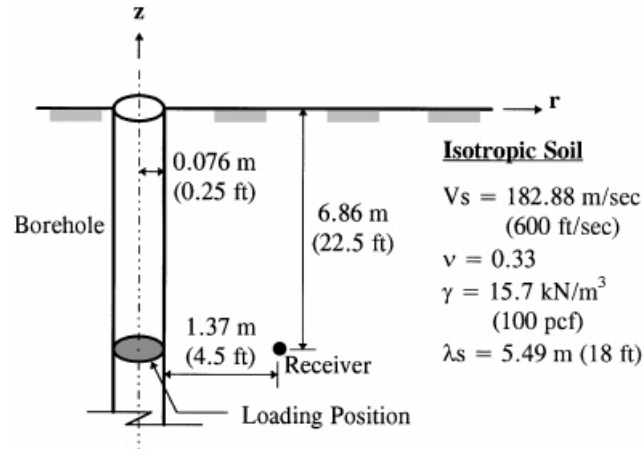


Figure 2. Geometry of the test and material properties

and  $\mathbf{H}^{-1}$  is the inverse of matrix  $\mathbf{H}$ . If the damping matrix is neglected, (6) becomes

$$\mathbf{U}_{t+1} = \Delta t^2 \mathbf{M}^{-1} (\mathbf{P}_t - \mathbf{K} \mathbf{U}_t) + 2\mathbf{U}_t - \mathbf{U}_{t-1} \quad (8)$$

This method is conditionally stable so that the time step  $\Delta t$  should be smaller than a critical value for stability. The critical step for a finite element system is obtained by dividing 2 into the maximum frequency  $\omega_{\max}$ .<sup>5</sup> To find the highest frequency for the critical time step of an element with  $n$  degrees of freedom, the forward iteration method was used. Using the central difference formula with a diagonal mass matrix eliminated the need to assemble the complete stiffness matrix of the system. Instead the displacements were computed separately at each node for each time step dividing the nodal forces resulting from the adjoining elements (computed element by element) into the associated nodal masses.

### CONVERGENCE STUDY

Convergence tests were performed changing the element size as a function of the predominant shear wavelength  $\lambda_s$ . Figure 2 shows the geometry of the test and material properties used for this study. The elements had square cross sections and the load was a sinusoidal impulse of half a cycle duration with a period of  $2T_d$  with  $T_d$  of 30 ms and amplitude of 14.6 N (3.28 lb). It should be noticed that the dimensions used are smaller than the actual ones in the practical application of the crosshole method and a relatively short duration of time is considered to avoid having reflections from the boundaries. They were selected to reduce the number of degrees of freedom and cost of computation. The mesh size of the finite element model used in the study was 21.3 m (70 ft) by 25.9 m (85 ft) in the horizontal and vertical directions. It should also be noticed that since linear elastic behaviour of the material was assumed, the results would be valid for very low levels of strain and thus very small amplitudes of the excitation. In this range, to obtain the results for another amplitude, it would be sufficient to multiply the published results by the appropriate constant.

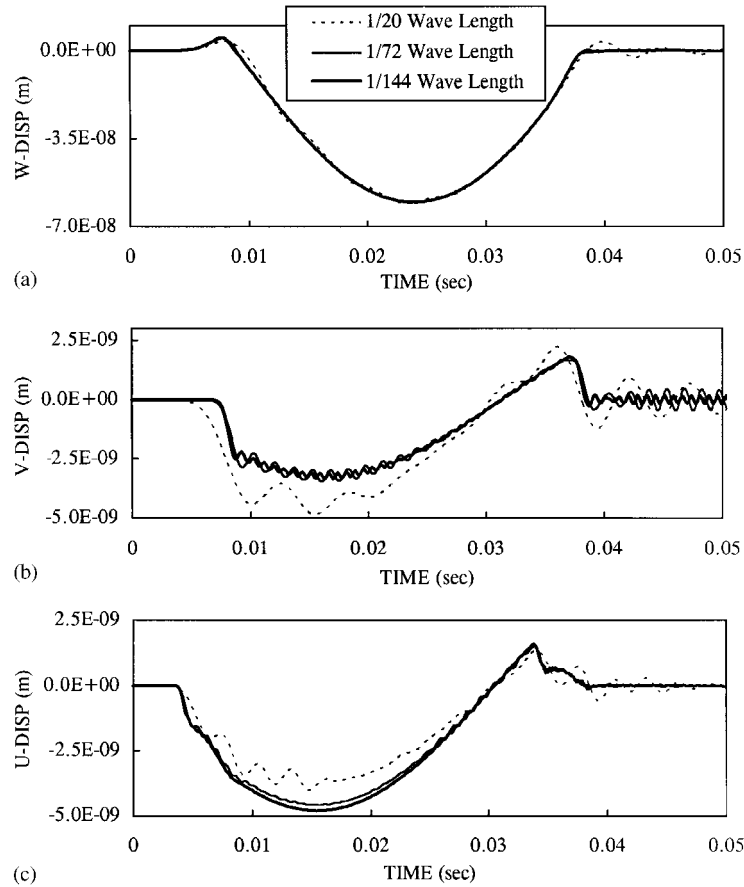


Figure 3. Effect of element size: (a) SV waveforms to VS force; (b) SH waveforms to PT force; (c) P waveforms to RE force

For the SV waveforms due to the downward shear force (VS force), convergence was achieved very fast as shown in Figure 3(a). For the SH waveforms due to pure torsion (PT force), shown in Figure 3(b), element sizes of  $\lambda_s/72$  and  $\lambda_s/144$  give very similar displacement responses, which implies that an element size of  $\lambda_s/72$  is accurate enough for practical purposes. It should be noticed that the solution with the finest mesh show still some high-frequency fluctuations which are a result of the discretization. The P waveforms due to the radial expansion or contraction (RE force) need an element size equal to or even smaller than that of the PT excitation as shown in Figure 3(c), but it does not result in as large spurious fluctuations. Although the radial expansion (RE force) and the vertical shear force (VS force) have both non-zero radial and vertical displacement components  $u$  and  $w$ , this study considers mostly the displacement in the direction of the applied load. The dominant displacement when the receiver is placed at the same level of the source occurs in the direction of the applied load.

Three impulse shapes, triangular, half sine and half sine square were used as shown in Figure 4 to investigate their effect on the displacement response. The source and the receiver were placed at a depth of 12.19 m (40 ft) with a horizontal distance of 3.05 m (10 ft). As shown in Figure 5,

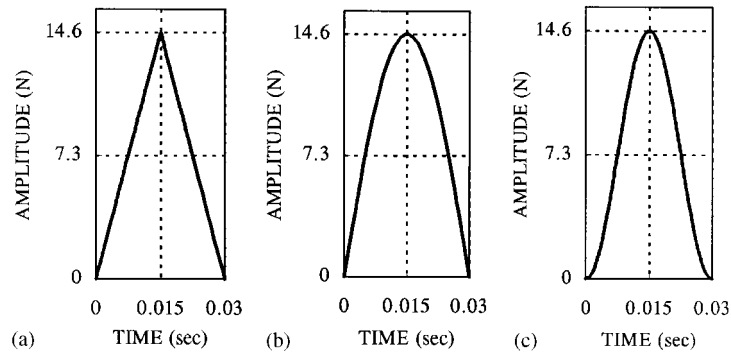


Figure 4. Impulse shapes: (a) triangular; (b) half a sine; (c) half a sine squares pulses

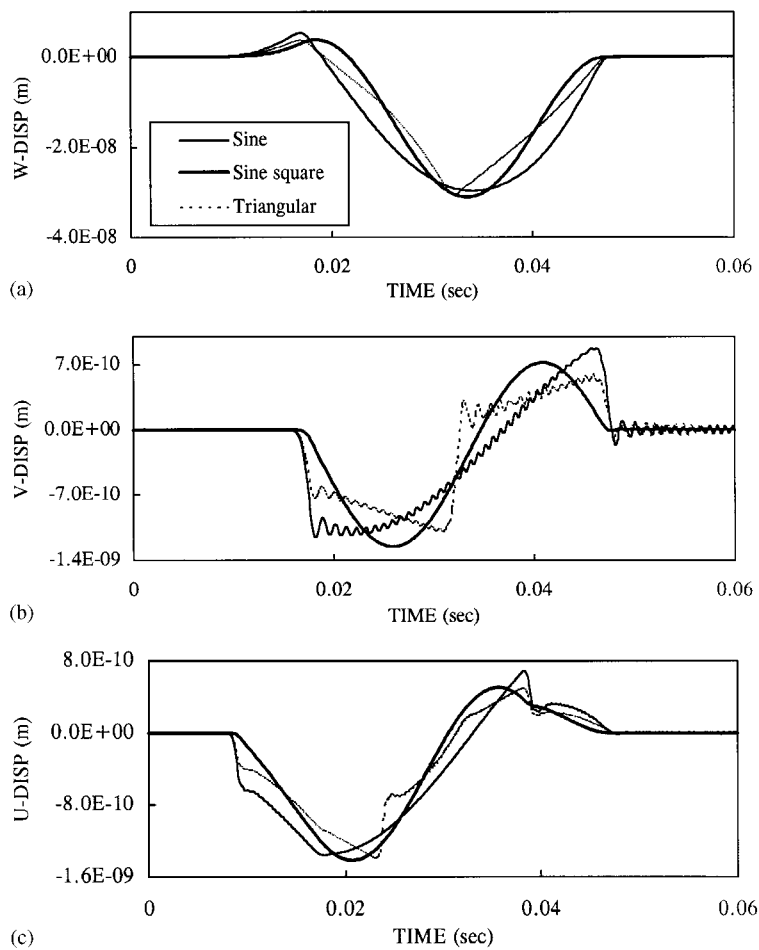


Figure 5. Effect of impulse shapes: (a) SV waveforms to VS force; (b) SH waveforms to PT force; (c) P waveforms to RE force

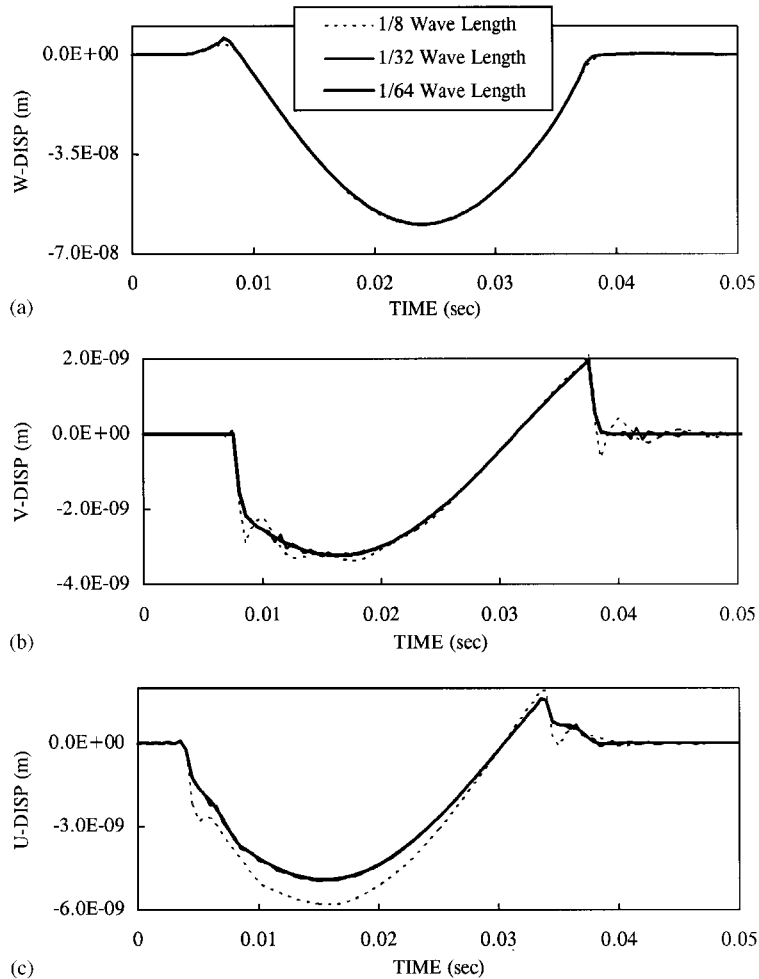


Figure 6. Effect of layer thickness: (a) SV waveforms to VS force; (b) SH waveforms to PT force; (c) P waveforms to RE force

a sine square impulse yields very smooth displacement records for all cases. The other impulses result in smooth responses for the SV waveforms but some small fluctuations for the *P* waveforms and many fluctuations for the SH waveforms. These fluctuations are numerical errors associated with the discretization. The shape of the impulse affects the high-frequency content and thus the numerical errors. The times when the main excursion starts, which are the times of arrival of the waves, are the same for the triangular and the sine pulses, but are harder to identify for the sine square pulse. The times of arrival of the waves can be obtained theoretically by dividing the distance into the wave velocity. The theoretical times of arrival are well matched with the times of arrival for the triangular and the sine pulse.

The results obtained through direct integration of the discrete equations of motion in the time domain were further verified comparing them to solutions carried out in the frequency domain, then converted to the domain using the Fast Fourier transform. The frequency domain solutions

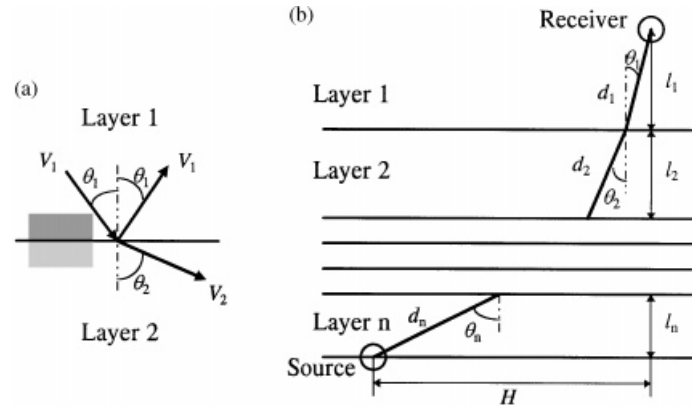


Figure 7. (a) Reflections and refractions of rays; (b) ray path model

were obtained using a consistent boundary to represent the soil around the borehole where the sources are applied<sup>6</sup> and using directly the discrete Green's functions for dynamic loads in a layered medium proposed by Kausel<sup>2</sup> with identical results (although in this case the existence of a borehole is ignored). The only discretization for this method was in the vertical direction.

The accuracy of the frequency domain solution depends only on the thickness of the discrete layers. The effect of the thickness of the layers is illustrated in Figure 6 using the model shown in Figure 2. As shown in Figure 6(a) for the VS loads the convergence is achieved very fast with excellent results even with a layer thickness of 1/8th of the wavelength although there is a small difference around the first peak. For the SH waveforms (Figure 6(b)) the overall shapes are similar but as the layer thickness decreases, the fluctuations decrease and very smooth shapes are obtained. For the P waveforms (Figure 6(c)) with the layer thickness of 1/8 of the wavelength the results are very bad, but the shapes converge as the layer thickness decreases. The final, converged, waveforms are in very good agreement with those obtained with the finite element model.

### RAY PATH MODEL

To identify the arrival times of the different waves in the records computed with the finite element model, a computer program was implemented based on the ray path model with curved paths. When a ray passes across the interface of two layers, it follows Snell's law as defined by

$$\frac{\sin \theta_1}{V_1} = \frac{\sin \theta_2}{V_2} \quad (9)$$

where  $\theta_1$  and  $\theta_2$  are the angles between the normal vector at the interface and the ray path in layers 1 and 2, respectively, as shown in Figure 7(a), and  $V_1$  and  $V_2$  are the appropriate propagation velocities in the two layers.

If  $H$  is the horizontal distance between the source and the receiver (Figure 7(b))

$$\sum_{i=1}^n l_i \tan \theta_i = H \quad (10)$$



where,  $l_i$  is the thickness of the  $i$ th layer and  $\theta_i$  is the angle between the normal vector of the interface and the ray path in layer  $i$ . Snell's law in (9) can be defined for the multilayered systems as

$$\frac{\sin \theta_1}{V_1} = \frac{\sin \theta_2}{V_2} = \dots = \frac{\sin \theta_n}{V_n} \quad (11)$$

where,  $V_1, V_2, \dots, V_n$  are the wave velocities of the various layers. The angles  $\theta_i$  can then be obtained solving (10) and (11). Knowing the values of  $\theta_i$ , the travel distances  $d_i$  of the ray in each layer can be obtained by

$$d_i = \frac{l_i}{\cos \theta_i} \quad (12)$$

Finally, the arrival time  $t$  can be calculated by

$$t = \frac{d_1}{V_1} + \frac{d_2}{V_2} + \dots + \frac{d_n}{V_n} \quad (13)$$

## ISOTROPIC SOIL DEPOSIT

### *General waveforms*

The waveforms due to the three different types of excitation were studied first for a single soil layer with the properties shown in Figure 2. The four noded, square cross section with a side length of 38.1 mm (1.5 in), axisymmetric finite elements were used and the mesh size was 21.3 m (70 ft) by 25.9 m (85 ft) in the horizontal and vertical directions. A sinusoidal impulse of half 8na cycle duration with a period of  $2T_d$  with  $T_d$  of 30 ms and amplitude of 14.6 N (3.28 lb) was used. As previously mentioned, in the crosshole method the motion is normally recorded at the same level as the source. Therefore, typical waveforms at the source level were investigated first. The results are shown in Figure 8. The times of arrival of the different waves obtained using the ray path model or in this simple case dividing the distance by the appropriate wave velocity are also marked in the results as P and S representing the times of arrival of P and S waves.

For the SV waveforms due to the VS excitation (Figure 8(a)), the motion starts at the time of arrival of the P wave although it is a motion perpendicular to the direction of wave propagation, and the initial displacements occur in the opposite direction to the applied force. The main excursion occurs at the time of arrival of the S wave in the same direction as the force and the motion becomes zero after the main peak. The time of arrival of the S wave corresponds to the point where the velocity (slope of the curve) changes sign. For the SH waveforms due to the PT excitation (Figure 8(b)) and P waveforms due to the RE excitation (Figure 8(c)), the motions start at the times of arrival of the S and P waves, respectively, and the main peaks occur in the directions of the forces. The motions are not, however, a single pulse. In all cases, the theoretical times of arrival of the main waves correspond to clear changes in the motions and are easy to recognize. The high-frequency fluctuation observed in the response to the PT excitation are again due to the discretization and could have been reduced by refining the mesh.

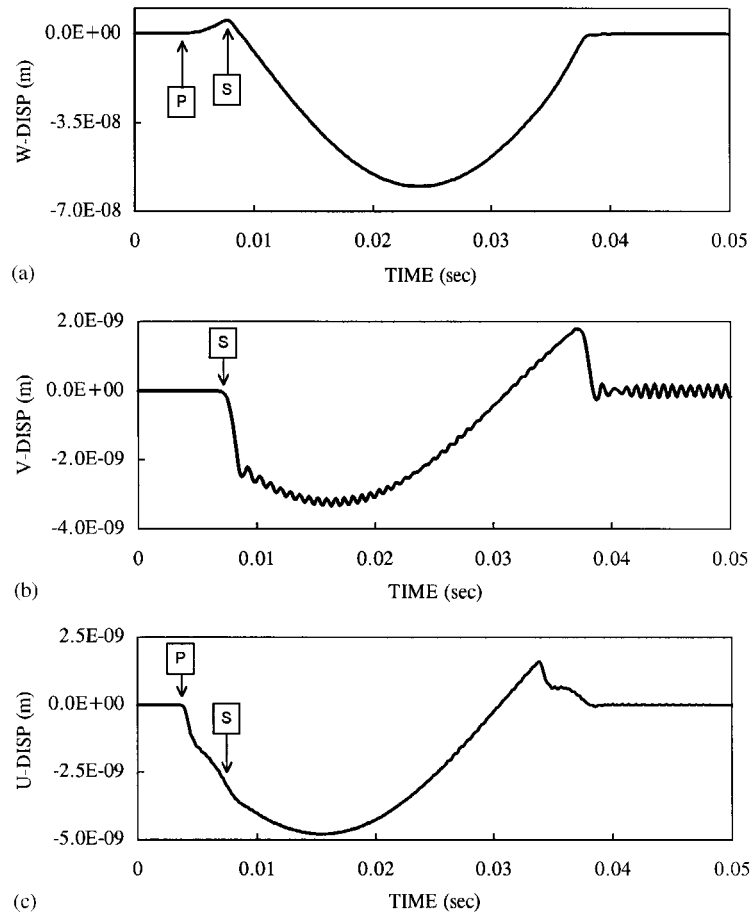


Figure 8. Typical waveforms at source level: (a) SV waveform to VS force; (b) SH waveform to PT force; (c) P waveform to RE force

### *Effect of vertical distance from the source*

To investigate the effect of distance from the source, various horizontal distances and receiver depths were considered with the source at 12.19 m (40 ft). For the PT load, the motion starts with the arrivals of the *S* waves and the shapes of the waveforms are very similar in all cases, so the results are now shown here.

For the VS load, at the level of the load (Figure 9(a)), the motion starts at the time of arrival of the *P* wave but the big excursion corresponds to the arrival of the *S* wave regardless of the horizontal distance. At a depth of 6.1 m (20 ft) (Figure 9(b)) the effect of the horizontal distance is more pronounced. When the distances are very short, the arrival of the *S* wave becomes hard to distinguish and the shapes are governed entirely by the motions associated with the *P* wave. As the distance increases, the arrival of the *S* wave becomes easier to identify and the shape of the waveform is governed by the motions associated with the *S* wave after it arrives. Therefore, to have clear SV wave arrivals at levels other than that of the load, the

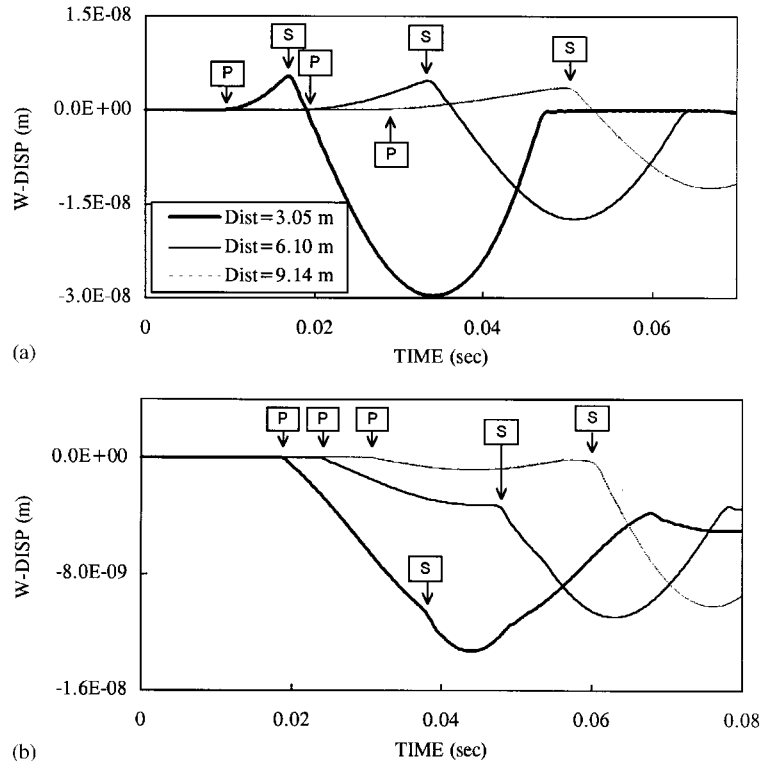


Figure 9. Effect of distance for SV waveforms to VS force: (a) at load level; (b) 6.1 m (20 ft) above load level

receivers should be located at a horizontal distance from the source of the same order of the vertical distance or larger.

For the RE load, at the level of the load (Figure 10(a)), the waveforms are governed by the arrivals of the P waves and the amplitude of the excursion decreases as could be expected as the horizontal distance increases. At a depth of 6.1 m (20 ft) (Figure 10(b)) the motion starts with the arrival of the P wave, but when the horizontal distance is short, the amplitude of the excursion associated with the arrival of the P wave is very small compared with the big excursions associated with the arrivals of the S waves. The arrival of the P waves is however easy to detect in all cases.

### EFFECT OF SOIL CROSS ANISOTROPY

In a cross anisotropic medium the propagation velocities of the P and S waves would be given by<sup>7</sup>

$$V_P^2 = l^4 V_{XX}^2 + n^4 V_{ZZ}^2 + 2l^2 n^2 \left( \frac{C_{13}}{\rho} + 2V_{XZ}^2 \right) \quad (14)$$

$$V_{SV}^2 = l^4 n^2 \left( V_{XX}^2 + V_{ZZ}^2 - 2 \frac{C_{13}}{\rho} \right) + (n^2 - l^2)^2 V_{XZ}^2 \quad (15)$$

$$V_{SH}^2 = l^2 V_{XY}^2 + n^2 V_{XZ}^2 \quad (16)$$

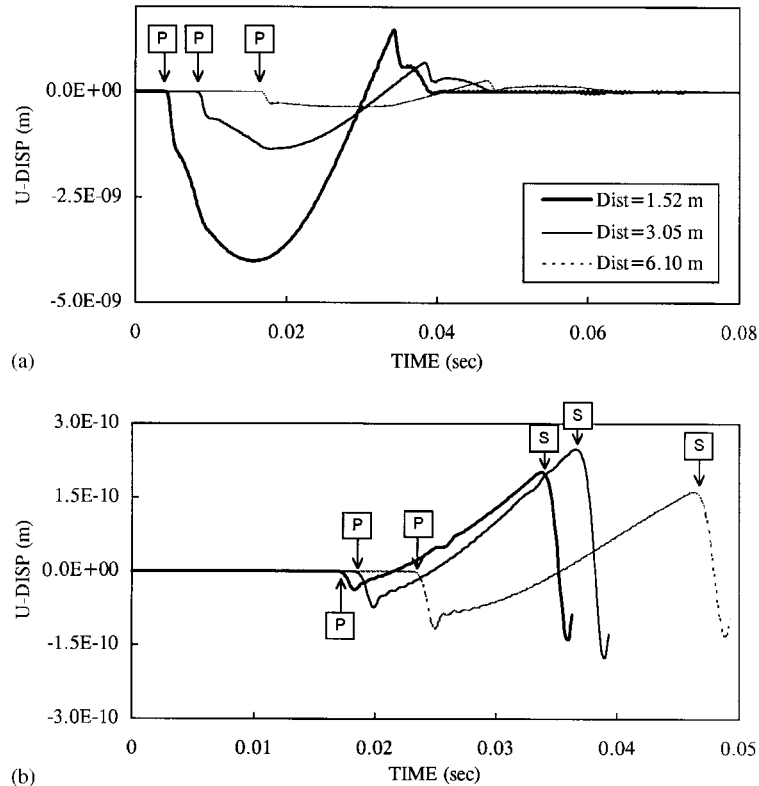


Figure 10. Effect of distance for P waveforms to RE force: (a) at load level; (b) 6.1 m (20 ft) above load level

where,  $l = \sin \theta$ ,  $n = \cos \theta$  and  $\theta$  is the angle between the normal of the isotropic plane and the direction of propagation.  $C_{13}$  is the fifth elastic constant defined by (2) and  $\rho$  is the mass density.  $V_{XX}$  and  $V_{ZZ}$  are the velocities of P waves propagating along the X and Z principal stress directions, respectively.  $V_{XY}$  and  $V_{XZ}$  are the velocities of shear waves propagating along the X principal stress direction with the particle motions in the Y and Z directions. Nine wave velocities can be defined in general in principal stress space, three for each direction. If the XY plane is the isotropic plane,  $V_{XX} = V_{YY}$ ,  $V_{XY} = V_{YX}$ ,  $V_{XZ} = V_{ZX}$ ,  $V_{YZ} = V_{ZY}$  and  $V_{XZ} = V_{YZ}$ .<sup>8</sup> Therefore, only  $V_{XX}$ ,  $V_{ZZ}$ ,  $V_{XY}$ , and  $V_{XZ}$  are needed in this case. There is, however, an additional constant  $C_{13}$  or  $C_{13}/\rho$ . A computer program was also implemented to find the first time of arrival of the waves using a curved ray path model in a cross anisotropic layered medium, making use of equations (14)–(16).

A single cross anisotropic soil layer was selected first with shear wave velocities of 182.88 and 228.6 m/s (600 and 750 ft/s) in the isotropic and vertical planes, respectively. The source was located at a depth of 12.19 m (40 ft), and the three receivers at depths of 0, 6.1 and 12.19 m (0, 20 and 40 ft) with a horizontal distance from the source of 2.51 m (8.25 ft). A half sine pulse with a duration of 30 m and an amplitude of 14.6 N (3.28 lb) was used. The results from the analyses and the theoretical times of arrival are shown in Figures 11–13. In these figures,  $P_x$  and  $P_z$  represent the times of arrival of the P waves propagating in the horizontal (isotropic) and vertical planes, respectively, and  $S_{xy}$  and  $S_{xz}$  represent the times of arrival of the shear waves

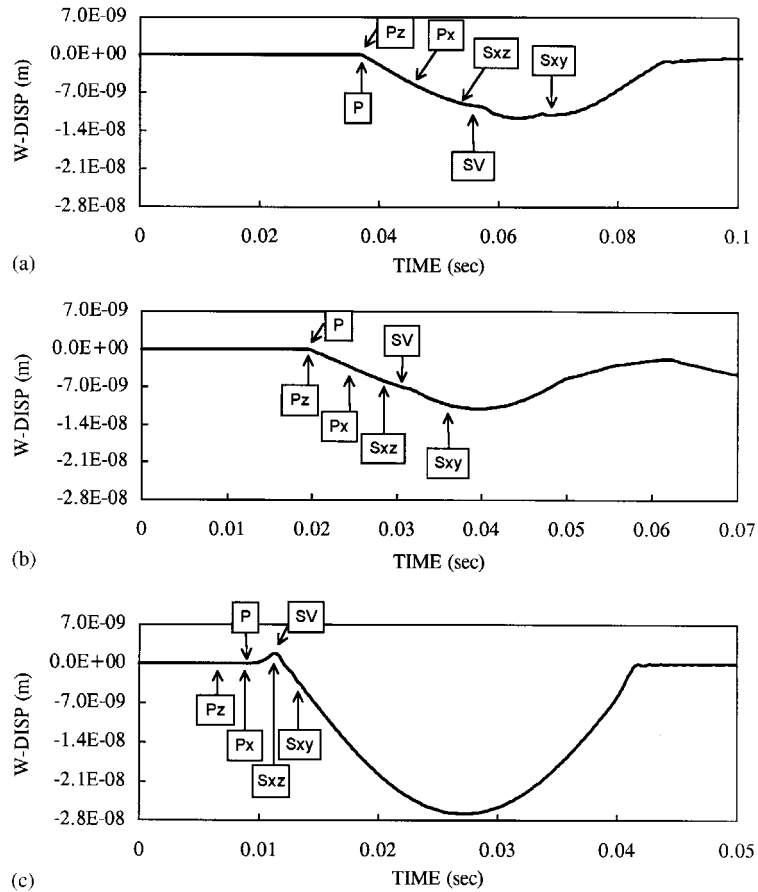


Figure 11. Times of arrival of waves for VS excitation: (a) at surface; (b) 6.1 m (20 ft) above load level; (c) at load level

corresponding to  $V_{xy}$  and  $V_{xz}$ . The times of arrival of the waves obtained by equations (14)–(16) are also marked as P, SV, and SH.

For the VS excitation case (Figure 11), the motion starts at the time of arrival of a P wave at all levels, but at the level of the load this time corresponds to  $P_x$  while it becomes  $P_z$  as the depth of the receiver decreases as predicted by (14). The main excursion at the load level starts at the time of arrival of the SV wave which corresponds to  $S_{xz}$ . As the depth decreases the time of arrival of the SV wave becomes hard to distinguish due to the small horizontal distance. It is somewhere between  $S_{xy}$  and  $S_{xz}$  and is given by (15). For the PT excitation case (Figure 12), the motion starts at the time of arrival of the SH wave, but it corresponds to  $S_{xy}$  at the load level and approaches  $S_{xz}$  as the depth of the receiver decreases. The high-frequency fluctuations in these figures are once again associated with the discretization and represent therefore numerical errors that could have been reduced. For the RE excitation (Figure 13), the motion starts with the arrival of a P wave. It corresponds to  $P_x$  at the load level and  $P_z$  at the surface. Another clear excursion can be observed at the time of arrival of the SV wave at all levels.

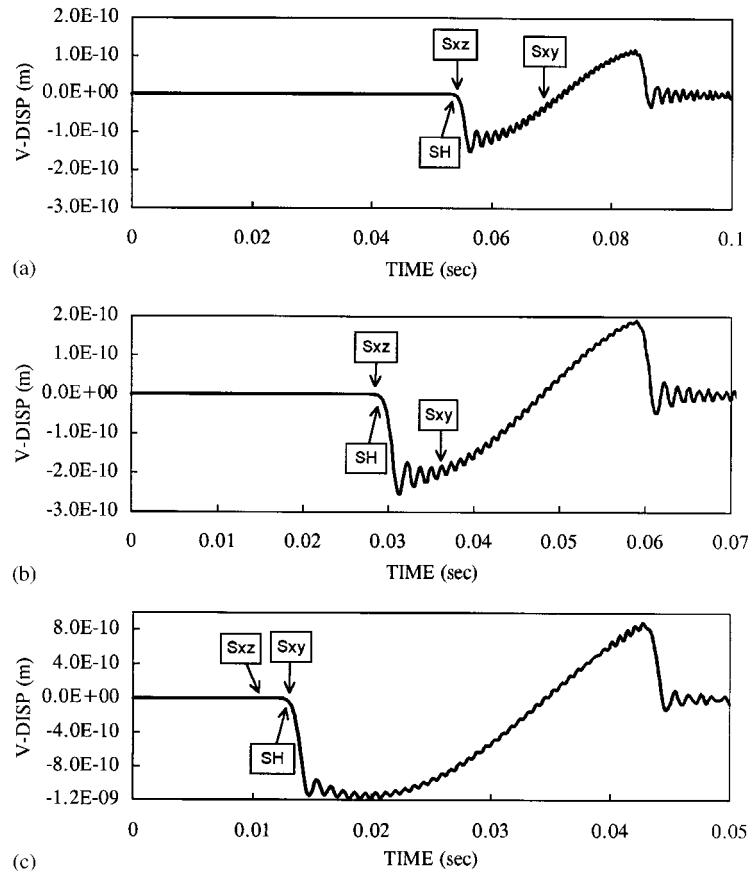


Figure 12. Times of arrival of waves for PT excitation: (a) at surface; (b) 6.1 m (20 ft) above load level; (c) at load level

A four-layered cross anisotropic soil deposit was considered next. Figure 14 shows the geometry of the test and the material properties are listed in Table I. The waveforms due to the VS excitation are shown in Figure 15. As in the isotropic case, the response starts at the theoretical time of arrival of the P wave at all receivers. The arrival of the shear wave is very clear at receiver 3 (at the road level) but it becomes hard to detect at the other receivers due to the relatively short horizontal distance compared to the vertical distance between the source and the receiver as previously explained. Figure 16 shows the results for the PT excitation with the expected frequency fluctuations due to numerical errors. At all levels, the response starts at the time of arrival of the SH wave from the ray path model. For the RE excitation, the motion starts at the time of arrival of the P wave at all receivers as shown in Figure 17. As the depth of the receiver decreases the excursion corresponding to the arrival of the P wave becomes very small and the big excursion occurs with the arrival of the shear wave. For all cases, the results obtained with the ray path model were in very good agreement with those of the finite element solutions as far as the times of arrival of the waves are concerned.

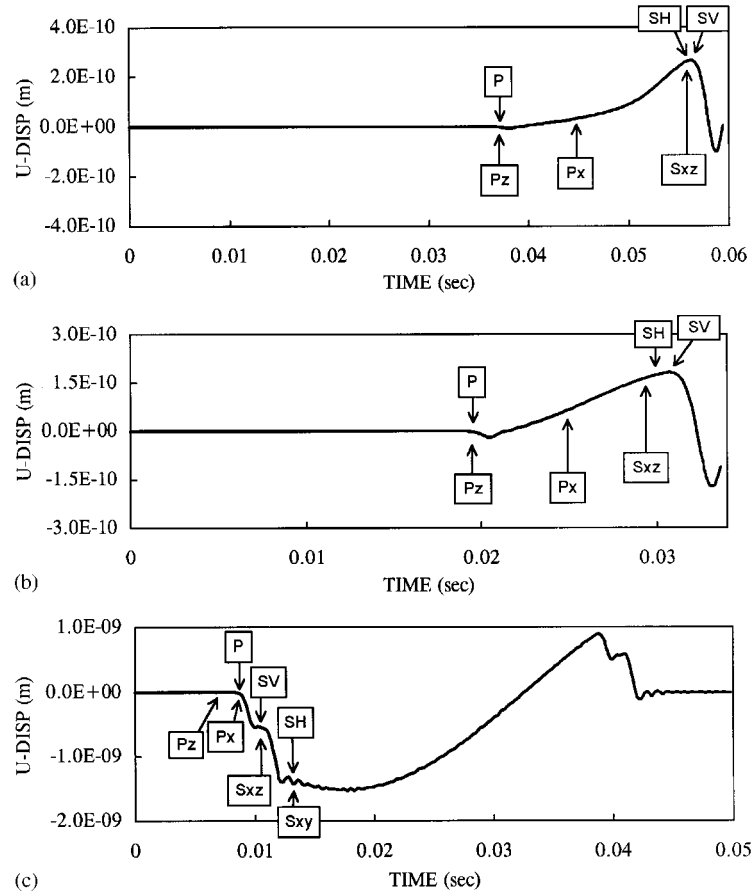


Figure 13. Times of arrival of waves for RE excitation: (a) at surface; (b) 6.1 m (20 ft) above load level; (c) at load level

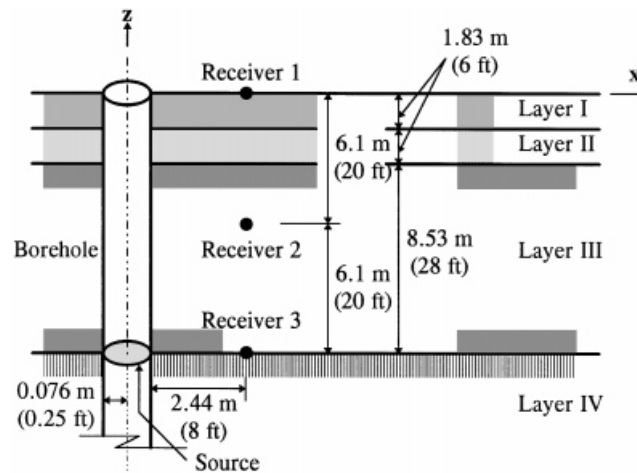


Figure 14. Four layered cross anisotropic soil deposit

Table I. Material properties for the four layered cross anisotropic soil deposit

Layers	$V_{XY}$ m/s (ft/s)	$V_{XZ}$ m/s (ft/s)	$V_{XX}$ m/s (ft/s)	$V_{ZZ}$ m/s (ft/s)	$C_{13}$ $10^8 \text{ N/m}^2$ ( $10^6 \text{ lb/ft}^2$ )
Layer I	122 (400)	134 (440)	201 (660)	226 (740)	0.42 (0.27)
Layer II	183 (600)	198 (650)	302 (990)	338 (1110)	0.94 (0.60)
Layer III	244 (800)	268 (880)	405 (1330)	451 (1480)	1.71 (1.09)
Layer IV	305 (1000)	332 (1090)	503 (1650)	564 (1850)	2.62 (1.67)

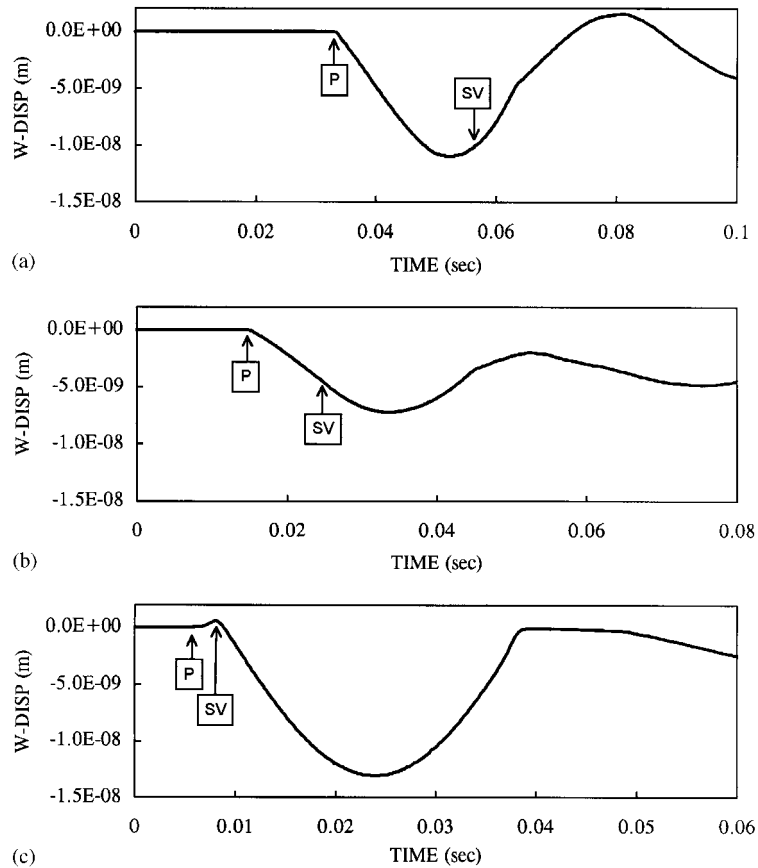


Figure 15. Waveforms for VS excitation: (a) at surface; (b) 6.1 m (20 ft) above load level; (c) at load level



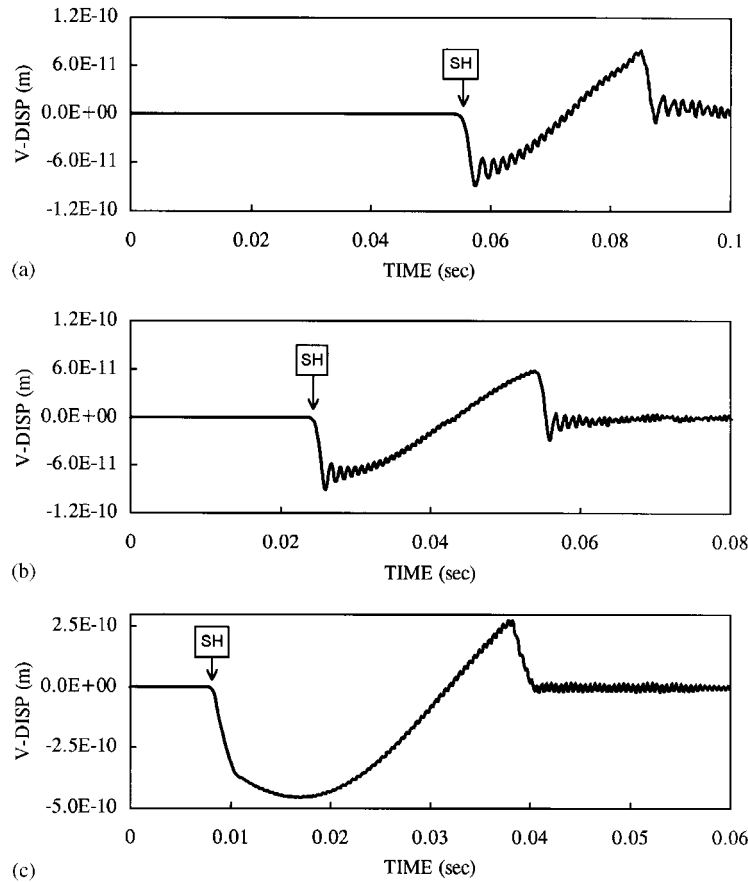


Figure 16. Waveforms for PT excitation: (a) at surface; (b) 6.1 m (20 ft) above load level; (c) at load level

## CONCLUSIONS

The crosshole method was simulated using a finite element model and the waveforms were investigated with three types of excitations representing PT (pure torsional), VS (vertical shear) and RE (radial expansion) forces. The times of arrival of the waves were also obtained using a ray path model accounting for curved (or polygonal) paths as well as possible reflections and refractions.

When dealing with the PT-type excitation, the waveforms have the same shape at all receivers and the arrival times are those associated with the SH wave velocity, which would be a function of the angle of propagation for a cross anisotropic material. For the VS excitation and recording the vertical displacement at the load level (as normally done in the crosshole method), the main component of the motion is associated with the arrival of SV waves although the motion starts at the time of arrival of the P wave. When motions are recorded at different depths as would be done in tomographic studies, as the vertical distance between source and receiver increases relative to the horizontal distance the arrival of the P wave becomes more pronounced while the arrival of the SV wave becomes harder to recognize. The opposite occurs when dealing with the RE type

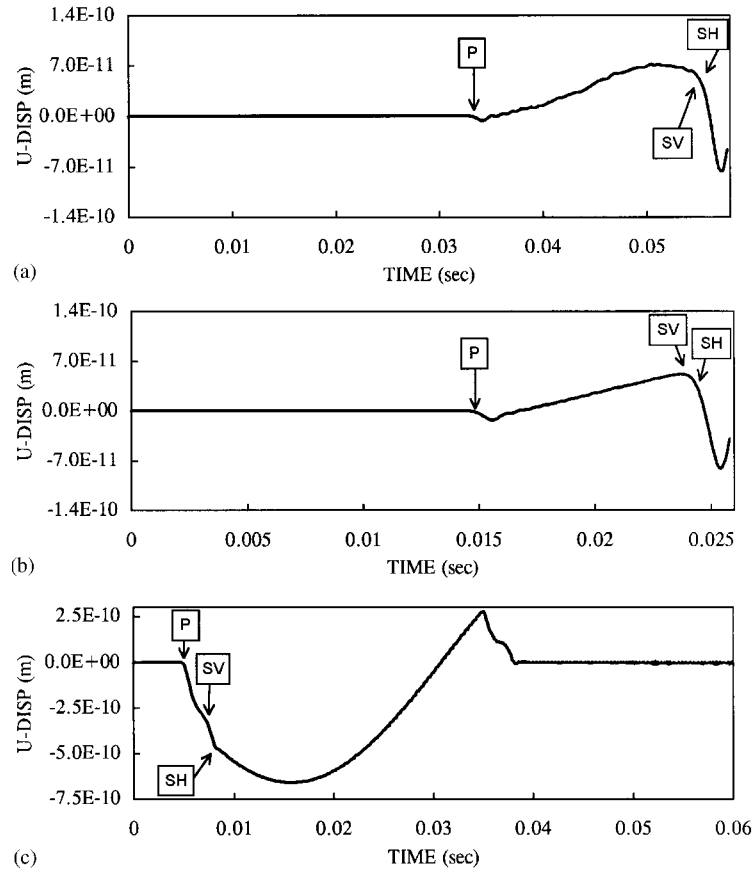


Figure 17. Waveforms for RE excitation: (a) at surface; (b) 6.1 m (20 ft) above load level; (c) at load level

excitation. The record of the radial displacement at the load level shows clearly the arrival of the P wave whereas no significant feature can be observed at the arrival times of the shear waves. At different depths, however, the excursion associated with the P wave becomes increasingly smaller and harder to detect and the main excursions are associated with the times of arrival of the shear waves. Yet the time of arrival of the P waves is still easy to recognize. It is thus important to be able to record the motions in more than one direction. The result obtained with a ray path model were in very good agreement with those of the finite element solutions as far as the times of arrival of the waves are concerned. The ray path model cannot provide, however, the complete waveforms.

The results of this study show that the interpretation of the wave arrivals in crosshole tomography is not straightforward and requires special care. This is particularly so when dealing with layered soil deposits.

#### ACKNOWLEDGEMENTS

The research described in this paper was sponsored by the Waterways Experiment Station of the U.S. Army Corps of Engineers and was part of a comprehensive study of the waveforms in

isotropic and cross anisotropic soils generated from the crosshole seismic method. Mr. Don Yule was the project supervisor.

#### REFERENCES

1. M. D. Fuhrman, 'Crosshole seismic tests at two northern California sites affected by the 1989 Loma Prieta earthquake', *Master Thesis*, Univ. of Texas at Austin, 1993.
2. E. Kausel, An explicit solution for the Green's functions for dynamic loads in layered media, *Rep. R81-13*, Massachusetts Inst. of Technol., Cambridge, MA 1981.
3. S. T. Liao and J. M. Roesset, 'Effects of anisotropy on the material properties inferred from downhole seismic tests', *Geotech. Engrg. Rep. GR95-2*, Univ. of Texas at Austin, 1995.
4. E. Hinton, T. Rock, and O. C. Zienkiewicz, 'A note on mass lumping and related processes in the finite element method', *Int. J. Earthquakes Engng. Struct. Dyn.*, **4**, 245–249 (1976).
5. K. J. Bathe, *Finite Element Procedures in Engineering Analysis*, Prentice-Hall, Englewood Cliffs, NJ, 1982.
6. E. Kausel, 'Forced vibrations of circular foundations on layered media', *Rep. R74-11*, Massachusetts Inst. of Technol., Cambridge, MA 1974.
7. S. M. Kim, S. T. Liao, and J. M. Roesset, 'Body waves in isotropic and cross anisotropic soils generated from crosshole seismic tests', *Geotech. Engrg. Rep. GR96-5*, Univ. of Texas at Austin, 1996.
8. S. H. Lee, 'Investigation of low-amplitude shear wave velocity in anisotropic material', *Ph. D. Dissertation*, Univ. of Texas at Austin, 1985.